PAPER • OPEN ACCESS

Large area scanning thermal microscopy and infrared imaging system

To cite this article: Jan Martinek *et al* 2019 *Meas. Sci. Technol.* **30** 035010

View the article online for updates and enhancements.

You may also like

Large area scanning thermal microscopy and infrared imaging system

Jan Martinek[1,2], **Miroslav Valtr**[1,3], **Václav Hortvík**[1], **Petr Grolich**[1], **Danick Briand**[4], **Marjan Shaker**[4] and **Petr Klapetek**[1,3]

[1] Czech Metrology Institute, Okružní 31, 638 00 Brno, Czech Republic
[2] Faculty of Civil Enginnering, Brno University of Technology, Žižkova 17, Czech Republic
[3] Central European Institute of Technology, Brno University of Technology, Purkyňova 123, 612 00 Brno, Czech Republic
[4] Ecole Polytechnique Fédérale de Lausanne (EPFL), Soft Transducers Laboratory (LMTS), Rue de la Maladière 71b, CP 526, CH-2002 Neuchâtel 2, Switzerland

E-mail: jmartinek@cmi.cz

CrossMark

Abstract

In today's highly integrated microelectronic systems there is a need for high-resolution spatial temperature measurement on chips. The resolution requirements are higher than the infrared imaging systems are capable of, and the investigated areas of the chips are often too large for most common scanning thermal microscopes. In this article we present two quantitative methods to acquire a thermal map with high resolution over a large area. We use two approaches: a noncontact method based on infrared radiation and scanning thermal microscopy (SThM). In both methods the expected thermal properties of the sample were thoroughly calculated and the prediction was in agreement with the experimental results. For the study of infrared radiation the composition of the sample together with the spectral sensitivity of the sensor were taken into account. In the SThM part, there were discrepancies based on unequal conditions during calibration and subsequent measurement. Using a finite element method simulation of the thermal field, the problem has been solved and successfully experimentally verified. For both methods a special sample with an embedded thermometer capable of being heated internally or externally was used.

Keywords: scanning thermal microscopy, large area SPM, finite element method

(Some figures may appear in colour only in the online journal)

1. Introduction

With increasing device integration in microelectronic systems and need for better heat management in modern integrated circuits, temperature mapping is facing novel challenges in terms of resolution and accuracy. The local power dissipation in microelectronic circuits is very high; moreover, it leads to creation of nanoscale hot spots that can have a crucial impact on device performance [1]. The ability to detect hot spots and to design circuits in order to reduce them is the basis of most efforts in the field of thermal management in integrated circuits. For all this it is important to have experimental tools available for surface temperature mapping at high resolution.

Traditionally, non-contact techniques based on electromagnetic field interaction were used for surface temperature measurements, starting with infrared imaging, monitoring black body radiation, through thermoreflectance, probing the sample optical properties' change with temperature, up to Raman thermometry, measuring the shift in Raman signal that also depends on local temperature [2]. The resolution of most optical techniques depends on the wavelength used for the measurement if a near-field principle is not used, so it can be in the order of hundreds of nanometers for visible light-based

techniques and up to tens of micrometers for infrared (IR) techniques. Out of these these techniques IR imaging is probably most general in terms of sample variability as it needs no sample preparation; however, it depends on local sample emissivity, has poor resolution [3] and is also subject to many other systematic errors and drifts. Nevertheless, radiation thermometry is used widely in the semiconductor industry as it is fast, non-contact, contamination-free and easily adaptable to various experimental situations.

As an alternative, a contact technique derived from the field of scanning probe microscopy (SPM) can be utilised, based on scanning the sample surface with a nanoscale thermometer. So-called scanning thermal microscopy (SThM) [4–6] achieves the highest spatial resolution in temperature measurements. This technique is based on the use of a local heater and/or temperature sensor, either in the form of a micro-fabricated probe or a very thin wire bent to form a probe. Scanning with this probe is performed using a conventional SPM feedback mechanism; the microscope can therefore measure sample topography and thermal properties at the same time. In the literature we can find many examples of SThM's use in mapping the temperature on active devices, in the fields of either electronics [7, 8] or optoelectronics [5].

When it comes to the traceability of thermal measurements, SThM is usually made traceable by calibrating the probe and associated electronics, e.g. using a heat bath. Even if this is done carefully, there are many potential systematic errors that can influence measurement, such as the effect of topography, probe self-heating or instrument drift during the measurements (which typically take quite long). For topographical artefacts, a null point technique minimizing the probe-sample heat flow [9] can be used. There also have been attempts to use more sophisticated measurement regimes separating the contact resistance from temperature data [8]. Other systematic errors can be minimized by careful experiment design and data processing, however the resulting uncertainties are still relatively high.

There is a large gap between the typical measured area scales and resolutions of infrared- and SThM-based temperature measurements. While a typical scanning probe microscope can hardly go beyond 100×100 μm^2 of the scanning range, with a spatial resolution far below one micrometer, devices like infrared cameras can image objects of virtually any size but with spatial resolutions only of tens of micrometers, even if provided with suitable optics. This makes comparison, or eventually traceability transfer, between the two techniques very hard. In this article we present an instrument designed for comparison of infrared imaging and SThM methods and for performing accurate temperature measurements using both methods. Based on a large area SPM scanner, we can go up to a scanning range of a few centimeters and, using a combination of multiple sensors, including SThM and IR imaging, we can obtain comparable data sets on millimeter scan areas, taking the best from both techniques—both the large area and high resolution.

In the SThM method the main complications arose from the Wollaston probe temperature distribution, which is very different during the calibration process and subsequent

measurement. The temperature field was calculated using the finite element method (FEM), and the corrected calibration data were successfully applied.

For infrared measurement, the key idea is to setup the radiation budget of the sample and the instrument; the complexity depends on the sample structure. Both methods, infrared- and SThM-based, were demonstrated using the same sample with a thin suspended membrane. The infrared radiation of the sample had to be calculated with respect to multiple layers of the sample, each layer being semi-transparent. Further, the spectral response of the sensor was strongly non-linear and the overall amplification of the apparatus was unknown. All these problems were finally solved by careful calculation of the radiation budget.

Both methods are rather complex and the model or calculation may be prone to errors. In order to validate the results, we have tested both methods using two sample heating modes: an active mode, achieved by passing an electrical current through the membrane, and a passive mode, using an externally heated sample holder. The conditions, like radiation budget or probe temperature distribution, are sufficiently different to verify understanding of the underlying physics.

2. The test sample

As a test sample we used a large-area hotplate developed at EPFL, shown in figure 1. The micro-hotplates were fabricated on a silicon substrate and consisted of a platinum (Pt) heater stacked between two silicon nitride insulators forming a suspended multilayered membrane. The membrane thermally isolates the heated area from the silicon chip frame and permits reducing the micro-hotplate power consumption. The fabrication process was started by RCA cleaning of 380 μm Si wafer and growth of a 500 nm-thick silicon dioxide (SiO_2) layer by wet oxidation method. Then, a 500 nm-thick low-stress silicon nitride film was deposited to form the membrane, and platinum (150 nm) with an adhesive layer of tantalum (50 nm) were patterned by lift-off process to make the heater. The heater area is 2.3×1.9 mm^2. Then, a 500 nm-thick silicon nitride layer covered the wafer and the contacts were opened. The membrane was released from the backside by dry etching of the silicon substrate and wet etching of SiO_2. The membrane size is 3.2×2.55 mm^2. For singulating chips, the wafer was covered by photoresist and then diced.

Two methods were used to find the temperature of the same sample. The first method was based on detection of infrared radiation and the second was SThM. The thermal field of the sample was rather uniform, which is good for calibration purposes but can not demonstrate the limit of the potentially high spatial resolution of SThM.

3. System setup

The system setup is shown in figure 2. The key component is a large-area, high-accuracy positioning system, NMM1 (nano positioning and nano measuring machine), made by SIOS, that is capable of positioning the sample in a volume
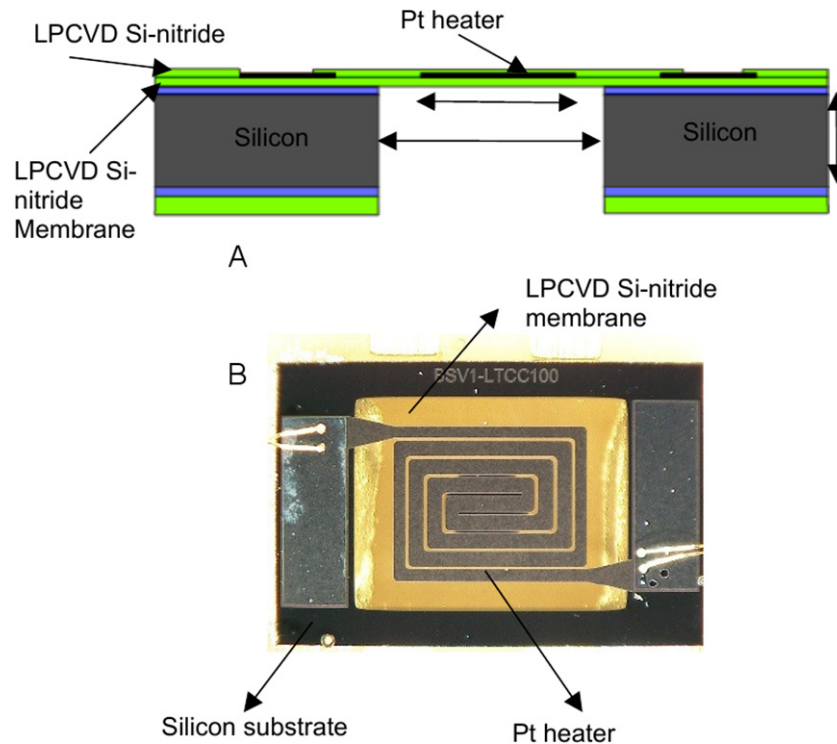
Figure 1. Test sample developed by EPFL: (A) schematic cross-section, (B) hotplate top-side view.

$25 \times 25 \times 5$ mm^3 [10, 11]. The high accuracy is provided by a combination of interferometric sensors and the use of thermally stable materials like Zerodur. The NMM1 device is combined with our custom-built measuring head that can perform both methods, SThM or infrared imaging, via a camera or mercury cadmium telluride (MCT) detector. The SThM probe was made of Wollaston wire and the signal processed using custom-built electronics. The infrared camera (Detector A) was used only for alignment purposes, while the measurement was done using the MCT sensor (Detector B). The same sample was measured using the same head by the two methods—infrared detection and then SThM.

4. Infrared imaging system

The first method for temperature measurement presented here is based on thermal radiation detection of a heated sample. The expected usage is in remote sensing of the spatial distribution of temperature in semiconductor chips. The temperature of the samples is in the range of room temperature up to 100 °C or slightly more. For such a temperature range, most radiated energy falls into the infrared band with a maximum of 8–10 μm. The sensor used to detect the radiation was a liquid-nitrogen cooled MCT sensor (Hamamatsu P9697-01), which is, according to its documentation, capable of responding to wavelengths in the desired range. However, the sensitivity is dependent on wavelength. To increase the signal-to-noise ratio (SNR) a chopper from Thorlabs with a lock-in detector (HF2LI from Zurich Instruments) was utilized; see figure 3.

Not only the sensor response varies with wavelength, but also the power radiated from the sample varies with wavelength. For an ideal black body the radiated power follows the

Planck distribution. However, the samples are not black body radiators and the Planck's curve must be multiplied by emissivity, which, again, is dependent on wavelength.

Therefore, the overall sensor response is proportional to the integral of three mutually multiplied curves: the sensitivity, the Planck's curve and the emissivity of the sample. As an example illustration, in figure 4 there is a sensitivity curve multiplied with a Planck's curve corresponding to 22 °C and 140 °C. The emissivity curve is not shown in the graph.

Two of these three curves are known. The most easy to obtain is the Planck's curve, which can directly be calculated. Then, the sensor's sensitivity is published in the datasheet by the manufacturer. However, no numerical data were available, only the PDF documentation with a sensitivity graph. After digitizing the graph, the values have been restored. The third curve (emissivity) is not so straightforward and will be discussed later.

Even if we know all three curves, still the amplification of the device is unknown. The proportionality constant remains the only unknown parameter and which depends mostly on the amplification of the device the sensor is connected to. To find the constant a calibration sample was made. It was based on an Edmund Optics 'Siemens star' target consisting of BK7 glass with a star-like metallic pattern. The BK7 glass was chosen for its well-known emissivity properties. The glass plate is heated to a desired temperature using an adjustable heater while the temperature is read by an attached Pt100 resistive thermometer.

It should be noted, however, that the overall output signal of the whole apparatus is not simply proportional to the value calculated as the response of the sensor. The reason behind this is related to the reflected radiation of surrounding objects
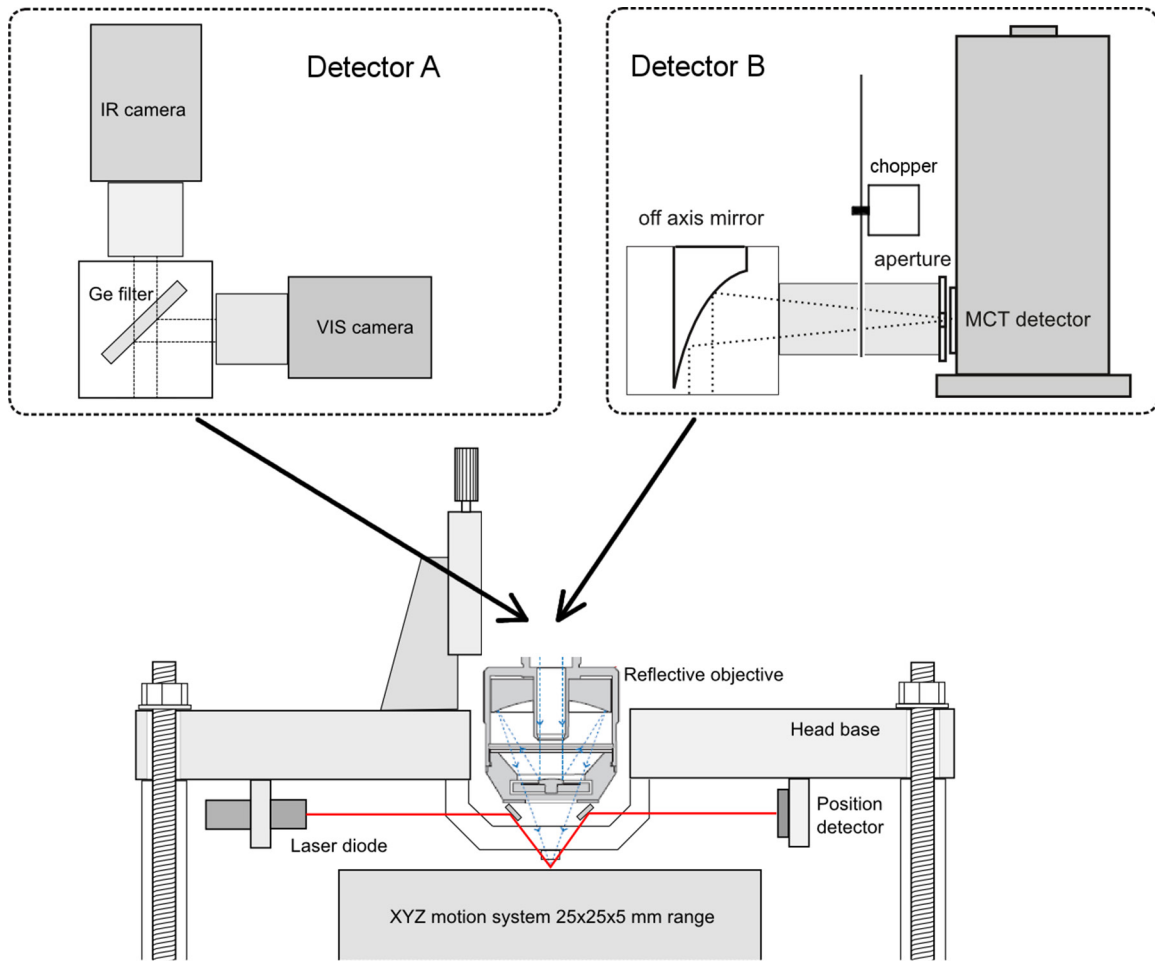
Figure 2. Large-area SThM/IR system setup, including (A) infrared + visible camera, (B) mercury cadmium telluride (MCT) detector and SThM head.

and also the chopper being the part of the device. These effects will be discussed in more detail later. The idea of finding an unknown multiplicative constant is still valid.

The calibration sample surface was heated to a series of temperature steps. At each temperature step the XY table scanned over a pre-selected area of the glass. The scanned area also contained a metallic part (the star pattern), which was useful for adjusting the focus and to ensure the scanned area was correct. For data processing only the pixels corresponding to the glass surface were taken into consideration and averaged.

Using such a procedure the output voltage of the device was found for each temperature step of a heated glass surface. The measured data is plotted on the graph of figure 5 together with a solid line representing least-squares fitting with a predicted function with the now-found multiplicative constant.

4.1. Emissivity of the multilayer test sample

The sample being tested should verify how capable the apparatus is of measuring surface temperature. In theory, we should follow the procedure for finding the emissivity using passive heating and subsequently find the temperature of the active, self-heating sample [12]. In our case this would not be
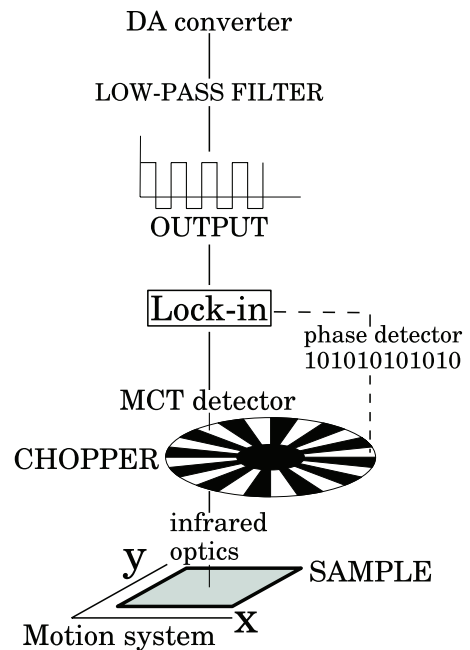

Figure 3. The sensor detects alternating radiation from the chopper fins and from the sample. The difference between these two sources is then amplified and demodulated.
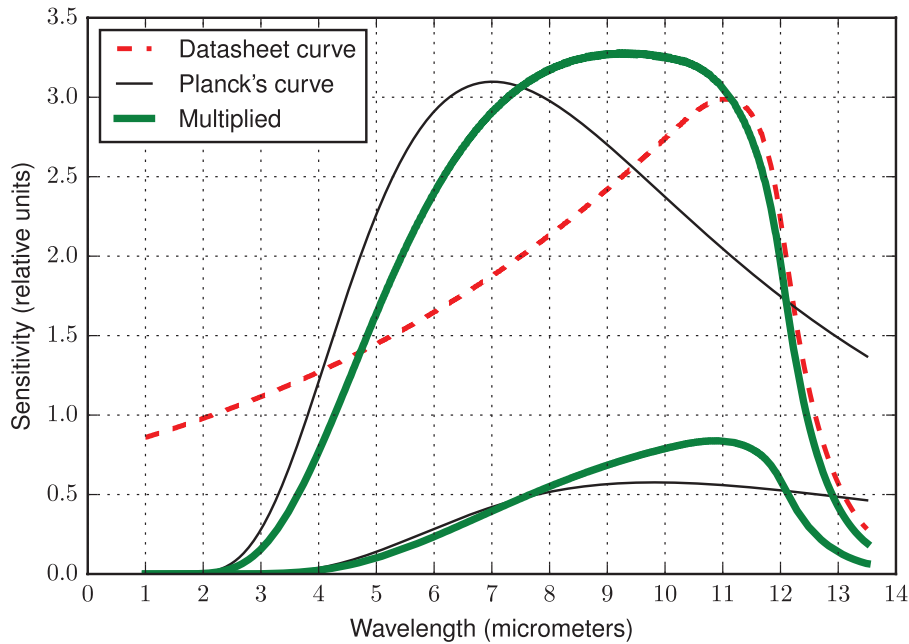
Figure 4. The MCT sensor sensitivity curve over wavelength was taken from its datasheet, digitized and multiplied by Planck's curve. There are two different Planck's curves for two temperatures, 22 °C and 140 °C, to demonstrate the temperature dependence. Moreover, the resulting curve should then be multiplied by the emissivity of the sample (not shown) and numerically integrated.
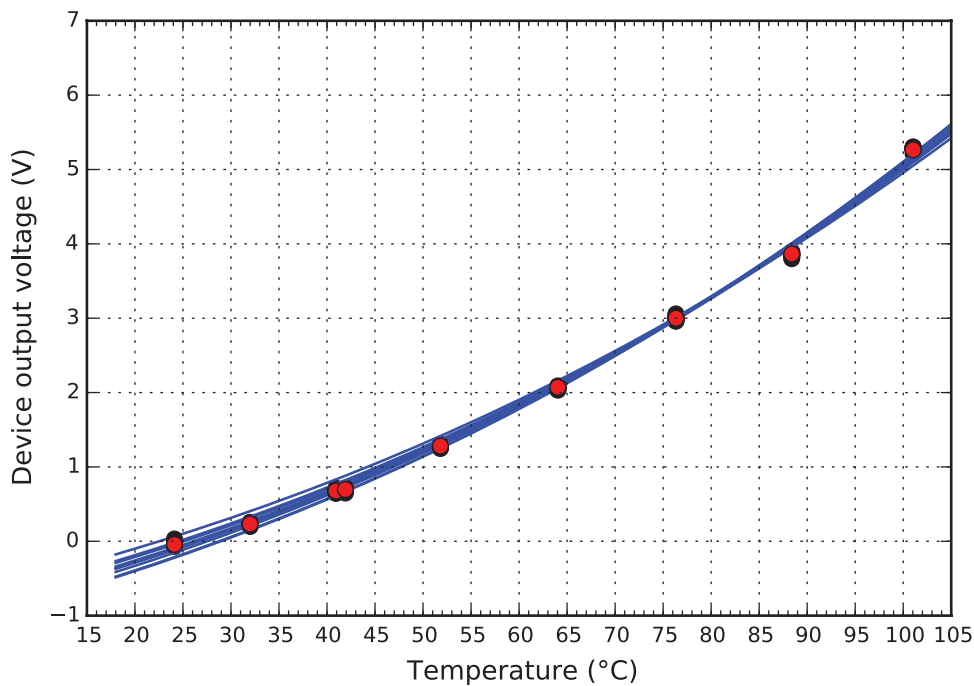

Figure 5. Measured output voltage from the infrared apparatus for several temperatures of BK7 glass substrate. Using the Monte-Carlo method and the glass emissivity $\varepsilon_{\mathrm{BK7}} = (0.93 \pm 0.02)$ the device amplification constant has been estimated for further calculations. The various blue curves in the graph represent the first ten iterations of the Monte-Carlo calculation.

sufficient because for purposes of evaluation we chose a deliberately more complicated sample than is common in electronic chips. The sample contained a void (air gap) between two layers while the top layer with a heating element was semi-transparent in the infrared band. The air gap represents a thermal insulation between the layers so the layers do not have the same temperature in the active mode, when only the top layer is heated and the bottom layer is in thermal contact

with the XY table of ambient temperature. On the other hand, in the passive mode the whole volume of the sample is heated, i.e. both layers have the same temperature.

This sample composition made measurement particularly difficult. The emissivity could not have been determined using passive heating because the bottom layer partially radiated through the top layer and the sensor would detect both intensities together. The only possibility in this case was to calculate all the
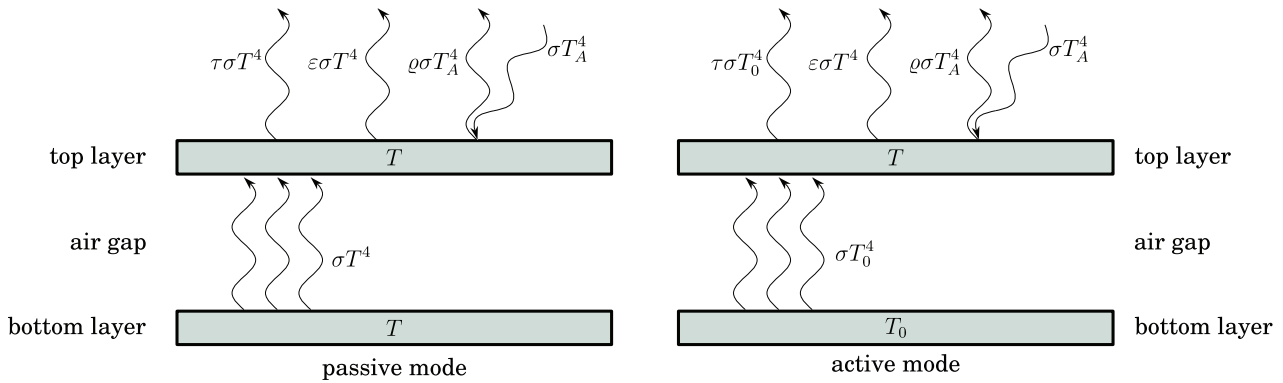
Figure 6. Thermal radiation from the sample consisting of two layers separated by an insulating air gap with the top layer being partially reflective and transparent.

optical characteristics of the top layer. The top layer was itself composed of three layers while the materials and thicknesses are known: silicon nitride (500 nm), platinum (150 nm) and again silicon nitride (500 nm). The absorptivity (=emissivity), reflectance and transmittance was determined in a range of wavelengths corresponding to the sensing range of the MCT detector.

The advantage of our sample is the integrated resistive thermometer. In the top layer there is a platinum coil which was used as a thermometer in passive mode or both as a heater and a thermometer at the same time in active mode. The resistance of the platinum coil was calibrated in an oven before other experiments were done. In passive mode a sensing current was sent through the coil, which was small enough not to increase the temperature. In the active mode the current was much larger, resulting in heating up of the top layer.

4.2. Radiation budget of a semi-transparent sample

As already explained, the response f of the MCT detector depends on its spectral sensitivity $s(\lambda)$ together with the Planck's curve and the emissivity function $\varepsilon(\lambda)$ of the surface being studied. Of course, the Planck's curve depends on temperature and so does also the response function. The main formula indicating the principle would be

$$f(T) = A \int_{\lambda_1}^{\lambda_2} s(\lambda)\, \varepsilon(\lambda)\, \frac{2\pi h c^2}{\lambda^5 \left(\exp \frac{hc}{\lambda kT} - 1 \right)} \, \mathrm{d}\lambda$$

where A is a multiplicative constant related to amplification of the device. The k, h, c are the Boltzmann constant, Planck constant and speed of light, respectively. The integration limits should be from zero to infinity, but the sensitivity function in the datasheet is plotted only from 1 μm to 13.5 μm (denoted as λ_1 and λ_2) and we assume the function to be zero outside this interval.

In simple terms, the radiation intensity could generally be denoted as usual σT^4, as would be the result of a solely integrated Planck's curve. Multiplication by a constant (i.e. emissivity) would represent the behaviour of a gray body. This approach is incorrect in our situation as the sensor response is not the same thing as radiation intensity. Anyway, for the case of brevity, the simplified approach has been used in figure 6 to illustrate the radiation budget of the two-layer sample.

Transmittance, reflectance and absorptance (emissivity) functions have been calculated for the top layer. With this information we can conclude the total response of the sensor as a sum of each response corresponding to each radiation source. On the left part of the figure 6 there is the passive mode in which both layers have the same temperature T. We assume there are three sources of radiation. First, the bottom layer radiates through the top layer, but only a fraction passes through according to the transmissivity τ. Second, the top layer thermally radiates itself while having an emissivity ε. Third, the ambient objects' radiation reflects from the surface with respect to its reflectivity ϱ [13]. But here the ambient objects are limited to the sensor itself, which detects reflection of its own. The set of mirrors are adjusted so that the smooth surface of the sample is perpendicular to the optical axis. Due to the fact the sensor is cooled by liquid nitrogen, its radiation is very low, but it has been considered in the calculation anyway.

A similar approach could be used to describe the right part of the figure 6 corresponding to the active mode. The differences should be clear from the picture. In the analysis we also mentioned the glass surface measurement, which was used to find the multiplicative constant A. There is no picture and radiation budget of the setup, because it is much easier and should be clear from the context.

The radiation budget described above is important for any non-opaque sample (i.e. non-zero transmissivity) in the infrared band. The idea is not specific to our complicated sample.

4.3. Optical chopper

The presence of an optical chopper must also be taken into account when considering the radiation budget. In order to enhance the stability and SNR, an optical chopper was placed between the sample and the sensor which alternately covers and uncovers the optical path while the sensor repeatedly detects the radiation of the sample and the radiation of the chopper fins back and forth. The chopper was deliberately made of a material with high emissivity in order to suppress the stray reflections of ambient objects. It is worth noting that commonly used black-finish metal choppers are highly unsuitable due to high reflectivity in the infrared band.

Table 1. The resulting temperature evaluated from infrared measurement compared with the reference embedded RTD thermometer in the membrane.

Mode\temperature	Measured by IR	RTD reference
Passive (sample heated externally)	93.0 ± 1.6	94.3
Active (sample heating internally)	93.6 ± 1.7	94.1

Due to rotation of the chopper, the output of the sensor is not a steady value but a square wave with a frequency equal to the chopper frequency. Its amplitude corresponds to the difference of radiation of the sample and that of the chopper fin. The amplitude is the main information acquired from the device and it is reconstructed from a noisy signal using a lock-in detector; the subsequent low-pass filter is pictured in figure 3. The output DC voltage is directly converted to pixel values of the generated image. Negative values of the output voltage are possible when the sample radiates less than the chopper.

4.4. Results

At first, the whole setup was tested using a sample made of BK7 glass with known emissivity $\varepsilon = 0.93$. The glass sample was heated to a series of temperature steps. For each temperature the output value was found as an average over a homogeneous area of the sample scanned with a resolution of 60×60 pixels. Using the data and the least squares method the multiplicative constant A of the whole apparatus was found. Next, the glass sample was replaced with the measured sample that has been described above. The sample was attached onto the same heater plate as the glass sample before. Then the measurement was carried out in two modes, passive and active. In both modes the actual temperature of the top layer was measured by means of the resistance of the embedded platinum heater. Since the infrared optical properties have been calculated and the multiplicative constant A had been found, the output voltage of the apparatus could be predicted for any temperature. Hence, the temperature could be found for the actually measured output voltage.

Additionally, in order to estimate the uncertainty of the whole procedure, the Monte-Carlo approach was used. The calculation was automated and repeatedly run with all the input parameters randomly shifted. The generated values of each parameter entering the computation followed the normal distribution statistics with the mean value and standard errors determined or estimated beforehand.

The first step was to calculate the multiplication constant A from the emissivity of the BK7 glass and the measured image thereof. The uncertainty of emissivity was estimated as 0.02. The same error was also used for the chopper emissivity. The error of image pixels was found statistically. To illustrate the spread of generated data using the Monte-Carlo method, the first ten curves are plotted in a graph in figure 5. The calculated constant A, each time slightly different, enters the second part

of the computation resulting in the temperatures of the sample in both active and passive modes.

From the output data the mean and standard error has been found statistically after several thousand repetitions. Both resulting temperatures together with the measured temperature are shown in table 1:

The measured temperature falls into a calculated interval for both modes. Again, ten randomly chosen calculated dependencies of output value with respect to temperature are plotted as graphs in figure 7 for the passive and active modes. The red lines on both graphs represent the actually measured output values and the reference temperature. The graphs confirm the usability of the method as both results are correct within the standard error.

5. SThM temperature measurement

The same sample was used to test the possibility of temperature measurement using a scanning thermal microscope. Again, two modes of operation were used, passive and active. In the passive mode the sample is heated by a heater placed underneath and in the active mode the membrane in the sample is electrically heated. The membrane is in both cases also a temperature sensor, because its resistance is measured and recalculated to temperature according to a calibration curve acquired prior to measurement.

The membrane's resistance gives only one value of temperature, whereas we have many data points from the image acquired using SThM. In order to make these two temperatures comparable, the average value was taken into account. The area over which the average value was calculated covers just the platinum layer at the sample. This is especially important for the sample when in active mode because of the particularly non-uniform temperature. It should be noted that the calibration was done in a thermal oven where the whole membrane was heated uniformly.

5.1. Calibration of the scanning thermal microscope and the probe

The calibration is a process which results in a dependence of scanning thermal microscope's output on the temperature of the probe. The calibration was done using a thermal oven and using a calibration device. During calibration the probe was removed from the microscope's holder and enclosed in the thermal oven. The probe was still connected to the SThM device by the same wires in order to preserve conditions. The whole volume of the Wollaston wire was heated and the results are well defined. However, the procedure is different from actual measurement when only the apex of the probe is in contact with the sample. This disadvantage was partially mitigated in the second calibration when a special calibration device was used. The main parts of the device were an embedded Pt100 sensor and a heater element. In this step the probe was installed into the scanning thermal microscope and scanned over the calibration sample in contact with its surface.
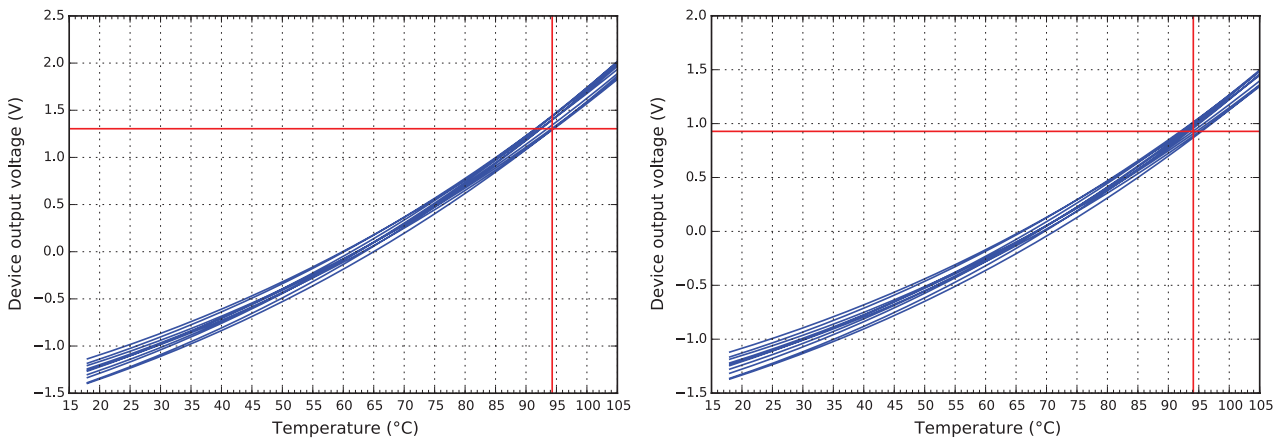
Figure 7. For both measurement modes, passive and active, the response curves of the infrared device were calculated. Using the Monte-Carlo approach the uncertainty of the final result was calculated. The blue curves represent an example of first ten calculations for slightly different input parameters. The measured temperature (red cross) correctly stays within the error interval.
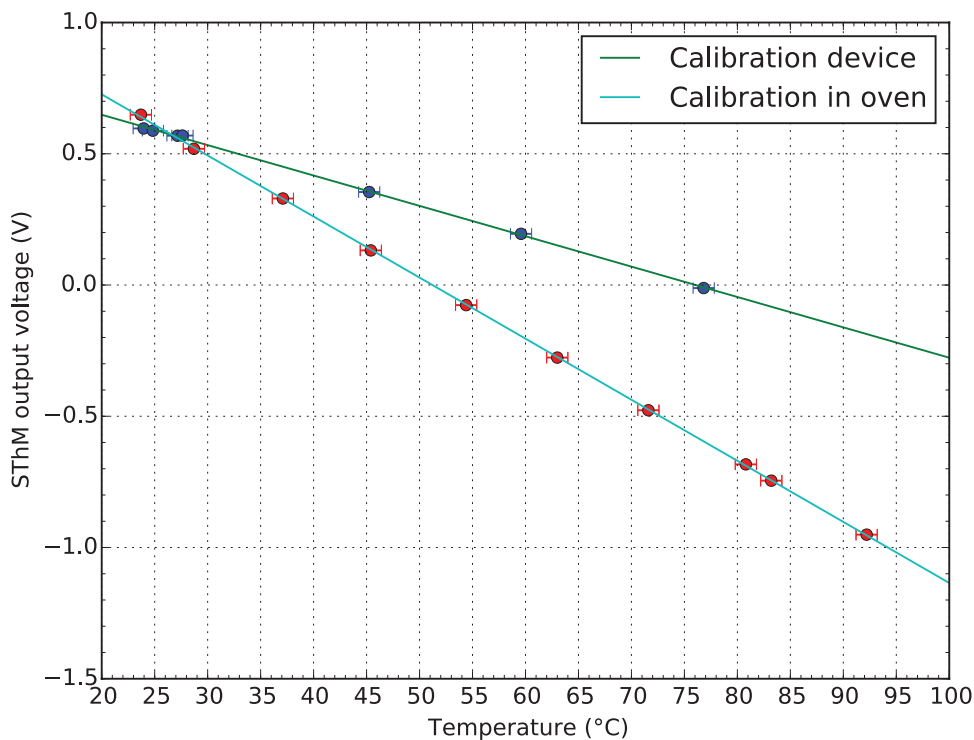

Figure 8. Two different ways of heating the scanning thermal microscope tip result in different calibration lines. Each calibration line represents the scanning thermal microscope output voltage with respect to the temperature applied to the probe.

Unfortunately, there is still no guarantee that the heated part of the Wollaston wire is the same as with the other sample [14].

Two calibration lines were obtained and their difference is obvious in the graph of figure 8. According to expectations, the slope of the line is much steeper when the temperature corresponds to the whole volume of the probe in the oven compared to the temperature of the calibration sample.

5.2. Modelling and calculation

For both modes, active and passive, there is a great disagreement between the temperature of the membrane and the temperature calculated using two different calibration lines. In order to explain this effect, a finite element method (FEM) model

was created. It consists of a bent wire with an apex nearly touching a multi-layered structure resembling the sample. The gap between the sample and the wire was set to 1 nm and empirically found the actual value does not have significant effect. The wire and the sample are surrounded by air. There are three materials used in the model: the air (thermal conductivity $k = 0.026$ W/m/K), the silicon nitride ($k = 29$ W/m/K) and the 90/10 platinum/rhodium alloy ($k = 29$ W/m/K, electrical resistivity at 20 °C $\varrho_{20} = 1.88 \cdot 10^{-7}$ Ωm and its thermal coefficient $\alpha = 0.0017$ K^{-1}).

The next step was to calculate the thermal field using the FEM. We assumed the prevalent heat transport to be the thermal diffusion, which can be modelled using Poisson's equation. This assumption was based on the fact the probe is
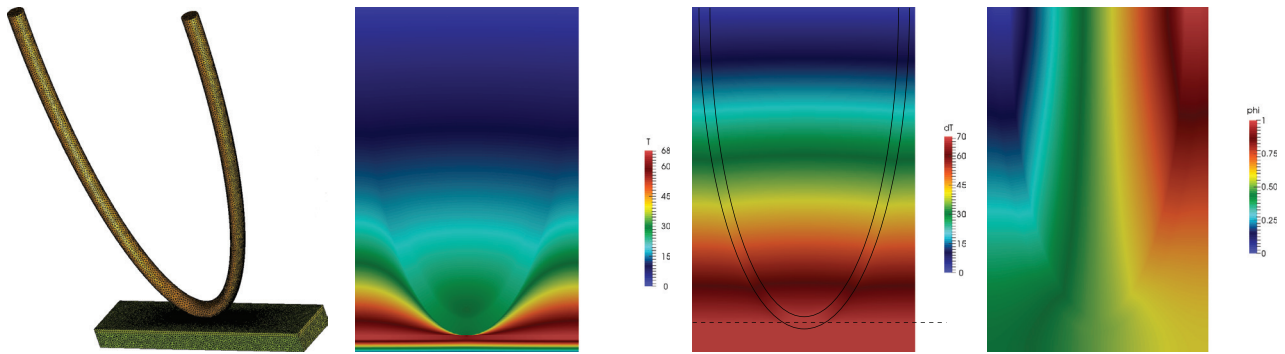
Figure 9. Using the finite element method the resistance of heated Wollaston wire was calculated. On the left there is the wireframe model of the geometry. The next image represents the temperature field in the active mode, followed by the passive mode. The right image is the resulting potential field from which the electrical current flow and resistance were calculated.

made of Wollaston wire, therefore being rather large. In the case of the most modern SThM probes, the nanoscale heat transfer effects would have to be taken into account [15].

After the temperature was found, the electrical resistance in each point of the wire was set according to the thermal coefficient of electrical resistivity and the temperature at the given point. The electrical resistance of the wire was therefore non-homogeneous and the highest value corresponds to the highest temperature. Then another FEM task was performed to find the spatial distribution of the electrical field under the assumption that the ends of the wire are kept to a potential difference of 1 V. At a cross-section of the wire the gradient of potential was calculated and multiplied by the local conductivity to get the electrical current density. The current density over the cross-section of the wire finally leads to electrical current. From Ohm's law the resistance of the wire is easily calculated.

The above procedure for calculating the electrical resistance of the wire was performed for four different modifications of thermal field representing the two calibration modes (using a thermal oven and calibration device) and two measurement modes (active and passive) according to the experimental work. All such data acquired from FEM simulation were further processed in the same way as the real data. Each temperature of the passive or active sample results in a calculated electrical resistance. The electrical resistance was recalculated back to temperature in accordance with the slopes of both virtual calibration lines.

Since the data from the FEM modelling are processed in the same manner as the experimental data, the results should mutually agree, but the temperature found is still incorrect due to different conditions during the calibration and the measurement. However, according to the FEM simulation the incorrect calibration line slope can be fixed and the new resulting temperatures should agree with the real temperature of the membrane.

5.2.1. Modelling of calibration in oven. The temperature of the whole wire was set to a constant value as it would be in the oven. The resistance could have been found analytically as the geometry is quite simple and the thermal field homogeneous. Despite this, the value was calculated using a FEM in order to take into account possible imperfections in the 3D mesh, which is the same in all other models. The resistance can easily be recalculated for any other temperature.

5.2.2. Active sample modelling. The membrane, which is the top-most layer, is heated by electric current and in the model is configured as a volumetric heat source with a constant power density (in watts per cubic meter). The temperature field in the membrane is in general not homogeneous, especially right beneath the probe because the probe conducts the heat away. However, further from the probe the temperature levels out, which is a good sign the computation domain is large enough. We assume the highest temperature in the computation domain represents the average temperature of the membrane. In figure 9 in the second picture from the left there is a cross-section of the temperature field. It should be evident that the average temperature of the Wollaston wire is much lower than the temperature of the membrane. This is an explanation why the resistance of the wire can not be directly recalculated to the temperature of the membrane.

5.2.3. Modelling of calibration device or passive sample. In both these situations we assume the heat source is large enough to heat up a significant part of the probe apex. In the model the bottom part of the whole geometry is set to a constant temperature. The membrane is heated to the same temperature as the air underneath, the air immediately above and also partially the tip apex. The thermal field is shown in figure 9 in the third picture from the left. The actual horizontal plane, representing the upper boundary of the heated objects, is somewhat unclear. In the simulation the boundary has been iteratively found to represent the best fit with the measured data. The same idea was used to model both the calibration device or passive sample only with a different thermal boundary. If the position of the thermal boundary plane is measured from the very apex of the tip, then for the calibration device the best results were found for 3 µm and for passive mode 4.5 µm. This is in agreement with the fact the heater for the passive sample is physically larger than the calibration device. It is worth noting the radius of the Wollaston wire is 2.5 µm.

5.3. Results

For each mode, active and passive, the output value was acquired from the SThM image. Figure 10 shows an example of the measured topography and the thermal signal image.
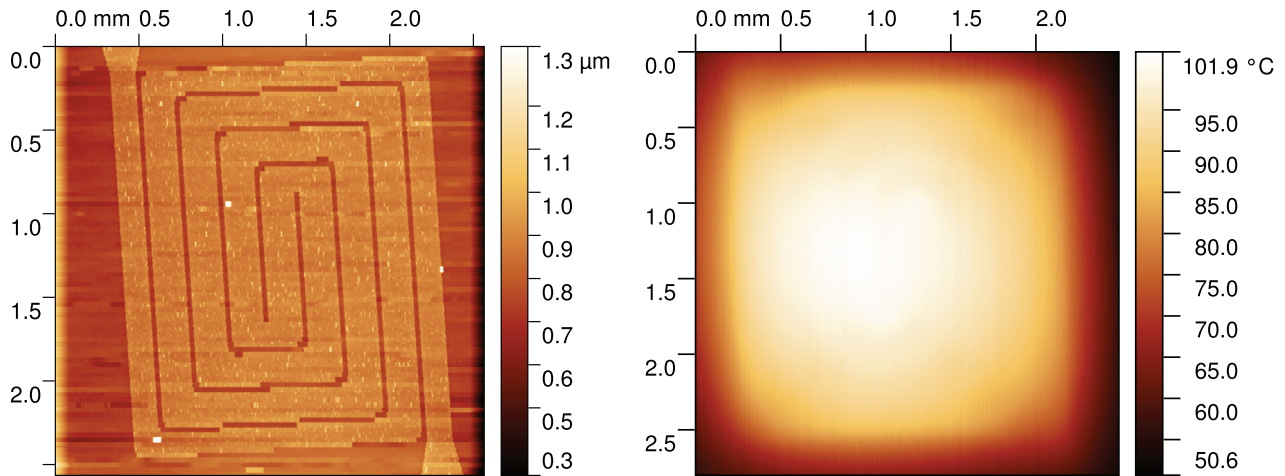
Figure 10. An example of a large-area SThM result, topography (left) and temperature (right). In this case the sample was in active mode only when the thin membrane was heated and its resistance corresponded to 90.4 °C. The resulting temperature scale was calculated from the calibration line from a thermal oven, and the slope of the line was corrected using data from FEM simulation.

Table 2. Uncorrected measurement results for two calibration modes. The T_{oven} corresponds to the SThM probe calibrated in the thermal oven, $T_{cal.device}$ is for calibration using a special sample.

	RTD reference	T_{oven}	$T_{cal.device}$
Passive	92.9	60.24 ± 0.34	94.18 ± 0.69
Active	90.4	38.19 ± 0.40	49.87 ± 0.73

Table 3. Measurement results compared with results of numerical model.

	T_{oven}	$T_{oven-model}$	$T_{cal.device}$	$T_{cal.device-model}$
Passive	60.24 ± 0.34	60.41 ± 0.50	94.18 ± 0.69	94.53 ± 0.50
Active	38.19 ± 0.40	38.28 ± 0.50	49.87 ± 0.73	50.04 ± 0.50

Table 4. Corrected measurement results for two calibration modes.

	RTD reference	$T_{oven-corr}$	$T_{cal.device-corr}$
Passive	92.9	91.99 ± 1.7	93.80 ± 1.8
Active	90.4	91.21 ± 5.4	90.00 ± 5.5

Because there are two calibration curves, one from the oven and one from the calibration device, there are four results which can be calculated as a resulting temperature of the membrane. Table 2 summarizes the results: it is evident that in three cases out of four the calculated temperature is completely wrong compared to the correct temperature of the sample (membrane). The main reason for the disagreement is what we mean by temperature [16]. The temperature of the membrane (RTD) is not the same as the temperature of the whole probe. The whole probe has the same temperature in all its volume when put into the thermal oven but not during the scanning process in SThM. Moreover, the average temperature of the probe calculated from its resistance is different from the reference temperature of the membrane.

For this reason the calculated temperature should not be compared to the temperature of the sample. It should rather be compared to the values obtained from the modelling. If the understanding of the physics behind the heat flow is correct, then the calculated temperatures should be in agreement; see table 3.

In all four combinations of the calibration process and the measurement mode the results are correct within the intervals of error. The uncertainty of the results obtained using FEM was estimated from many (more than 100) different meshes used in simulation. Moreover, from each simulation two results were obtained as there are two usable cross-section areas of the wire, one for electrical current inflow, the other for outflow. Due to numerical errors these may slightly differ. The precision of FEM was quite satisfactory, but the sensitivity (i.e. temperature change of resistance) is quite low

and therefore more prone to errors. Moreover, each calculated temperature comes from calibration and measurement, so there are two simulations for each result. All these factors were taken into consideration, yielding an uncertainty estimate of ± 0.5 degree.

5.4. Experimental data correction based on FEM results

The same simulation can be used to find the corrected slope of the calibration lines. These new calibration lines were used to find the temperatures and the results are now correct in all four combinations. The values measured using the membrane as a RTD thermometer are well within the uncertainty interval; see table 4. The corrected calibration line was also used to calculate the temperature map shown on figure 10 on the right. Due to the simplicity of the test sample only one FEM calculation was sufficient to obtain the equation, which is valid for all the data points acquired by SThM.

For more complicated heterogeneous samples with complex topography it might be necessary to calculate a FEM model for each pixel individually. This process is very computationally demanding, though feasible [17].

The temperature was found for all the points of the image, but only the average value could be compared to that measured using the membrane acting as a RTD thermometer. For this reason, only one value for each mode is presented in table 4.

The average value lies between the minimum and maximum temperature in figure 10.

Despite all the results being correct within their respective uncertainty interval, it should be noted that in the beginning there was one particular thermal oven used for all calibrations—either with the SThM probe or the membrane in the sample acting as RTD. In all calculations or estimates the absolute uncertainty of the calibration process in the thermal oven was not taken into account. The main goal is to correctly simulate the heat flow in various situations. Neglecting the thermal oven repeatability errors is actually a more stringent condition due to the fact all the intervals are then narrower.

For the purpose of absolute temperature measurement the uncertainty ± 1 °C of the thermal oven must be taken into account.

6. Conclusions

Two methods have been presented for measurement of the spatial temperature map of a sample consisting of a thin membrane which can be heated by electrical current or using an external heater. In both these modes (active and passive) the membrane itself works as a pre-calibrated RTD thermometer. One of the methods is based on detection of the infrared radiation (IR) of the sample. Using a sensitive mercury cadmium telluride (MCT) detector, infrared focusing optics, chopper and lock-in detector, an image of the heated sample is obtained. The whole device was calibrated using a BK7 glass with known emissivity. When the overall radiation budget had been taken into account together with the spectral response of the sensor, the resulting calculated temperature agreed with the correct temperature. All the uncertainties of the input parameters were processed using a Monte-Carlo approach to find the final uncertainty interval of the temperature.

The second method used for measurement of the temperature on the surface of a sample was based on scanning thermal microscopy (SThM). The device with a probe attached was calibrated using two approaches, using a thermal oven and using a calibration sample with known temperature. Both calibration lines differ significantly. They were used to find the temperature from SThM data corresponding to the active and passive modes of the sample. None of the four results was correct and the error was as much as 40 degrees. Further investigation and analysis using a finite element method (FEM) revealed very different temperature fields in all situations. From the calculated temperature distribution the overall electrical resistance of the probe was calculated as a part of a multi-physics FEM problem. Both calibrations and both modes of measurement were simulated. All four results from virtual calibration and virtual scanning finally agreed with their corresponding measured values. The main sources of the uncertainty were the fitting error from the scattering of calibration data points and the slightly variable results of FEM calculations at various computation parameters (i.e. mesh density).

When the model was found to be able to correctly simulate the whole procedure, the data from the simulation were used to modify the slopes of the calibration lines. Using the corrected calibration lines, a new set of four values for temperature was calculated. All four were in agreement with their corresponding RTD counterparts with respect to the uncertainty intervals.

From the calculation procedure and the results it should be obvious that estimating the average temperature of the probe could be very misleading and the electrical resistance of the probe does not depend only on the temperature at the apex.

ORCID iDs

Jan Martinek ![ORCID] https://orcid.org/0000-0002-7591-4101
Miroslav Valtr ![ORCID] https://orcid.org/0000-0002-7628-9184

References

[1] Pop E 2010 Energy dissipation and transport in nanoscale devices *Nano Res.* **3** 147–69
[2] Kim M M, Giry A, Mastiani M, Rodrigues G O, Reis A and Mandin P 2015 Microscale thermometry: a review *Microelectron. Eng.* **148** 129–42
[3] Gmelin E, Fischer R and Stitzinger R 1998 Sub-micrometer thermal physics: an overview on SThM techniques *Thermochim. Acta* **310** 1–17
[4] Pollock H M and Hammiche A 2001 Micro-thermal analysis: techniques and applications *J. Phys. D: Appl. Phys.* **34** R23–53
[5] Cahill D G, Goodson K and Majumdar A 2002 Thermometry and thermal transport in micro/nanoscale solid-state devices and structures *J. Heat Transfer* **124** 223
[6] Gomes S, Assy A and Chapuis P O 2015 Scanning thermal microscopy; a review *Phys. Status Solidi* a **212** 477–94
[7] Shi L and Majumdar A 2001 Recent developments in micro and nanoscale telemetry *Microscale Thermophys. Eng.* **5** 251–65
[8] Menges F, Mensch P, Schmid H, Riel H, Stemmer A and Gotsmann B 2016 Temperature mapping of operating nanoscale devices by scanning probe thermometry *Nat. Commun.* **7** 10874
[9] Chung J, Kim K, Hwang G, Kwon O, Choi Y K and Lee J S 2012 Quantitative temperature profiling through null-point scanning thermal microscopy *Int. J. Therm. Sci.* **62** 109–13
[10] Manske E, Hausotte T, Mastylo T, Machleidt T, Franke K-H and Jäger G 2007 New applications of the nanopositioning and nanomeasuring machine by using advanced tactile and non-tactile probes *Meas. Sci. Technol.* **18** 520–7
[11] Nanopositionier- und Nanomessmaschine https://sios.de/produkte/nanopositionier-und-nanomessmaschine/
[12] DeWitt D P and Nutter G D 1988 *Theory and Practice of Radiation Thermometry* (New York: Wiley)
[13] White D R and Saunders P 2008 A graphical method for calculating reflection errors in radiation thermometry *Int. J. Thermophys.* **29** 395–402
[14] Depasse F, Grossel P and Trannoy N 2004 Probe temperature and output voltage calculation for the SThM in A.C. mode *Superlattices Microstruct.* **35** 269–82

[15] Lefevre S, Volz S and Chapuis P-O 2006 Nanoscale heat transfer at contact between a hot tip and a substrate *Int. J. Heat Mass Transfer* **49** 251–8

[16] Wielgoszewski G, Sulecki P, Janus P, Grabiec P, Zschech E and Gotszalk T 2011 A high-resolution measurement system for novel scanning thermal microscopy resistive nanoprobes *Meas. Sci. Technol.* **22** 094023

[17] Martinek J, Klapetek P and Charvátová Campbell A 2015 Methods for topography artifacts compensation in scanning thermal microscopy *Ultramicroscopy* **155** 55–61